

Giant spin-orbit splitting of point defect states in monolayer WS₂

Wun-Fan Li,* Changming Fang, and Marijn A. van Huis

*Soft Condensed Matter, Debye Institute for Nanomaterials Science,
Utrecht University, Princetonplein 5, 3584CC Utrecht, The Netherlands*

(Dated: June 10, 2016)

The spin-orbit coupling (SOC) effect has been known to be profound in monolayer pristine transition metal dichalcogenides (TMDs). Here we show that point defects, which are omnipresent in the TMD membranes, exhibit even stronger SOC effects and change the physics of the host materials drastically. In this Article we chose the representative monolayer WS₂ slabs from the TMD family together with seven typical types of point defects including monovacancies, interstitials, and antisites. We calculated the formation energies of these defects, and studied the effect of spin-orbit coupling (SOC) on the corresponding defect states. We found that the S monovacancy (V_S) and S interstitial (adatom) have the lowest formation energies. In the case of V_S and both of the W_S and W_{S_2} antisites, the defect states exhibit giant splitting up to 296 meV when SOC is considered. Depending on the relative position of the defect state with respect to the conduction band minimum (CBM), the hybrid functional HSE will either increase the splitting by up to 60 meV (far from CBM), or decrease the splitting by up to 57 meV (close to CBM). Furthermore, we found that both the W_S and W_{S_2} antisites possess a magnetic moment of $2 \mu_B$ localized at the antisite W atom and the neighboring W atoms. All these findings provide new insights in the defect behavior under SOC point to new possibilities for spintronics applications for TMDs.

I. Introduction

The transition metal dichalcogenides (TMDs) are a member of the layered 2D van der Waals (vdW) materials, in which the atoms are bound by intra-layer chemical bonding and inter-layer vdW bonding. Among many other TMDs, the molybdenum dichalcogenides and tungsten dichalcogenides (MX_2 , $M=Mo$ or W , and $X= S, Se, \text{ or } Te$) are the group 6 branch of the whole TMD family and have attracted much scientific attention. Theoretically, the most stable structure of MX_2 consists of one layer of transition metal atoms sandwiched by two layers of chalcogen atoms with a prismatic coordination, forming the so-called 1H form¹. Due to the weak inter-layer vdW interaction, TMDs can be exfoliated from bulk into the few-layer or monolayer (ML) forms. When reducing the number of layers from bulk to ML, the band gap of TMDs evolves from an indirect band gap to a direct band gap with an increased gap size due to quantum confinement^{2,3}. The layer-dependent tunability of the electronic structure together with other distinct physical properties of ML TMDs make them promising candidates of applications in fields like electronics, optoelectronics, spintronics and valleytronics, sensing, and catalysis⁴⁻⁷.

There are two effects governing the band structure (BS) of MX_2 , namely crystal field (CF) splitting and spin-orbit (SO) splitting (Δ_{SO}). These two effects strongly affect the electronic properties of MX_2 and influence in particular the d bands of the transition metal.

According to crystal field theory, the five formerly degenerate d bands of the transition metal will split in energy if the transition metal is bonded to other ligands (the chalcogen atoms in our case), and the pattern of the energy splitting is dependent on the metal-ligand coordination geometries. For ML MX_2 in the 1H phase, the transition metal is surrounded by six chalcogen atoms in a trigonal prismatic coordination (Fig. 1). Consequently, the d bands split according to their orientations - the more they are along the direction

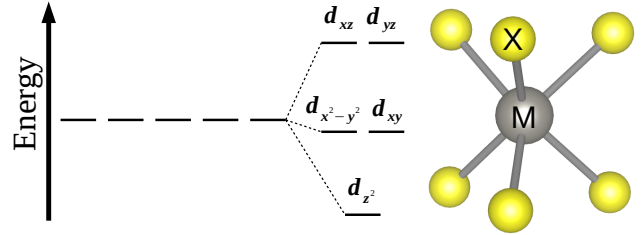


FIG. 1: Schematic of the energy splitting of the transition metal d bands under the crystal field. The coordination is trigonal prismatic.

of the M-X bond, the higher in energy they will be due to the electron-electron repulsion with the X orbitals. As shown in Fig. 1, the d_{z^2} orbital is the lowest in energy, and the $d_{x^2-y^2}$ and d_{xy} orbitals are higher in energy. The d_{xz} and d_{yz} orbitals are the highest in energy^{8,9}. The Supplemental Material (SM) shows the decomposed band structures of both bulk and ML WS₂ which illustrate the CF splitting of the d bands (Figures S3 and S4). The order of increasing energy is $d_{z^2} < d_{x^2-y^2} = d_{xy} < d_{xz} = d_{yz}$ for both bulk and ML WS₂, as expected.

The spin-orbit coupling (SOC) effect in MX_2 materials has been discovered in the last few years¹⁰⁻¹³. In bulk MX_2 , the system possesses both the space inversion symmetry ($E_{\downarrow}(\vec{k}) = E_{\downarrow}(-\vec{k})$) and time inversion symmetry ($E_{\downarrow}(\vec{k}) = E_{\uparrow}(-\vec{k})$). The net result is spin degeneracy in reciprocal space when no external magnetic field is present: $E_{\downarrow}(\vec{k}) = E_{\uparrow}(\vec{k})$. However, in the case of ML MX_2 , because of the lack of space inversion symmetry, the spin states are expected to split under SOC. Especially, the band splitting can be as large as 463 meV for the valence band maximum (VBM) of ML WS₂ at the K point in the first Brillouin zone¹³. Based on symmetry arguments^{10,13}, for ML MX_2 only the orbitals with magnetic quantum number $m_l \neq 0$ will participate SO splitting.

Furthermore, because the X atoms are rather light, their p orbitals are not affected by the SOC effect. Lastly, as indicated in the BSs of ML WS_2 in the SM (Fig. S4), the VBM and conduction band minimum (CBM) are dominated by the d_{z^2} ($m_l = 0$), d_{xy} ($m_l = -2$) and $d_{x^2-y^2}$ ($m_l = 2$) orbitals. As a result, only the d_{xy} and $d_{x^2-y^2}$ orbitals will have the SO splitting.

Besides the novel physical properties of pristine TMDs, atomic point defects are omnipresent in the materials. Furthermore, adatom adsorption and doping on ML MX_2 is especially achievable by virtue of their 2D surface nature. Both the naturally occurring and chemically or physically introduced point defects in MX_2 will extensively modulate the physical properties such as charge transport, magnetism, optical absorption, and absorbability¹⁴⁻³⁰, thus control the applicability of the material. The crucial role of point defects has triggered many studies to investigate their behavior in ML MX_2 . Liu *et al.* identified the atomic defects and visualized their migrations on ML MoS_2 ³¹. Komsa *et al.* found that electron beam irradiation generates sulfur monovacancies (V_S) and also cause these defects to migrate and aggregate^{32,33}. Zhou and *et al.* carried out a joint experiment and theory study and investigated several types of defects and their influence on the electronic structure of ML MoS_2 synthesized by chemical-vapor-deposition (CVD)³⁴. Among the single vacancy, vacancy complexes and antisite complexes, they found that the V_S is the predominant point defect. First principles calculations confirmed that V_S has the lowest formation energy among all the defect kinds. Hong *et al.* did a systematic study which shows the route-dependency of predominant point defect types³⁵. In ML MoS_2 synthesized by CVD and mechanical exfoliation (ME), V_S is the only dominating point defect, whereas in ML MoS_2 fabricated by physical-vapor-deposition (PVD), the antisites Mo_{S2} and Mo_S are the dominant point defects. They also found that the Mo_S antisite possesses a local magnetic moment around the Mo defect site. From the theoretical perspective, several exhaustive works have been done to study the point defects systematically by virtue of the density functional theory (DFT)³⁶⁻³⁸. Their results predict that in ML MX_2 , the V_S and sulfur interstitial S_i have the lowest formation energy.

Despite the significance of SOC and point defects for ML MX_2 systems, to the best of our knowledge thus far no study has been conducted on the SOC effect on the electronic structure of defective ML MX_2 . Therefore, here we investigate how the SOC effect will change the band structure (BS) of ML MX_2 when different types of point defects are present. We chose systematically three categories of point defects: monovacancies (V_S and V_W), interstitials (S_i and W_i), and antisites (S_W , W_S , and W_{S2}). For conciseness, the ML WS_2 slabs containing these defects are abbreviated as: V_S - WS_2 , V_W - WS_2 , S_i - WS_2 , W_i - WS_2 , S_W - WS_2 , W_S - WS_2 , and W_{S2} - WS_2 , respectively. The relaxed structure of each point defect is shown in Figure 2. We chose WS_2 as a representative of the MX_2 family as the physical and chemical properties of all the MX_2 members are very similar, and thus the results of WS_2 are expected to be applicable to other MX_2 systems.

After describing the computational settings, we will first

discuss the formation energies of the selected defect species. We then chose V_S , S_i , W_S , and W_{S2} for further investigation of the SO defect state splitting. We found that SOC causes giant defect state splitting in the cases of V_S and W_{S2} , with the magnitude of the band splitting up to 194 meV for V_S and 167 meV for W_{S2} respectively. In addition, we also found that both W_S and W_{S2} antisites possess a magnetic moment around the antisite W atom, which is contrary to the previous study of MoS_2 ³⁵. The findings in this work provide a deeper insight in the point defect physics of MX_2 and will help developing potential applications of MX_2 in electronics and spintronics.

II. Computational details

All calculations were performed using the DFT code VASP³⁹⁻⁴¹ within the Projector-Augmented Wave (PAW) framework⁴². The exchange and correlation energies were described using the Generalized Gradient Approximation (GGA) formulated by Perdew, Burke and Ernzerhof (PBE)^{43,44}. The cut-off energy of the wave functions and the augmentation functions were 400 eV and 550 eV, respectively. The van der Waals correction with the optB88-vdW density functional⁴⁵ was used as at the beginning of this study the bulk WS_2 was also included⁴⁶. The supercell size of the ML WS_2 was 6×6 in the $x - y$ plane, and the vacuum along the z direction was larger than 16 Å. These dimensions of the supercell were sufficiently large to avoid the artificial defect-defect interaction. A Γ -centered $2 \times 2 \times 1$ k -mesh was used. The thresholds of energy convergence and force convergence were 10^{-4} eV and 10^{-2} eV/Å, respectively. We examined the SOC effect and found that it does not affect the structure but only influences the electronic properties of WS_2 , therefore we only included SOC after geometry relaxation to obtain the band structure (BS) and DOS for the systems. We first performed the geometry relaxation and total energy calculation with only vdW correction included (without SOC). Then we turn on SOC, and exclude vdW correction for calculating the electronic properties (BS and DOS) of the relaxed geometry. Spin polarized (SP) calculations were performed for every point defect species, and only the W_S and W_{S2} antisites were found to be magnetic due to their unpaired electrons. The initial geometry of each point defect configuration was chosen based on previous theoretical studies^{37,38}. The stringent setting described above guarantees a good convergence of defect formation energy within 0.01 eV.

In addition to standard DFT calculations, we also performed the more advanced hybrid functional (HSE06)⁴⁷ calculations for the defective ML WS_2 which shows defect state splitting under SOC (the V_S - WS_2 , W_S - WS_2 , and W_{S2} - WS_2). The goal of these HSE+SOC calculations is to investigate how HSE will affect the defect state splitting. The HSE calculations were performed on the DFT-relaxed geometries and we found that HSE relaxation gave almost identical geometries compared to traditional DFT. We set the fraction of Hartree-Fock exchange functional to 0.168 by fitting the calculated band gap of ML WS_2 to the experimental value. This fraction gives us a band gap of 2.04 eV, which is very close to the ex-

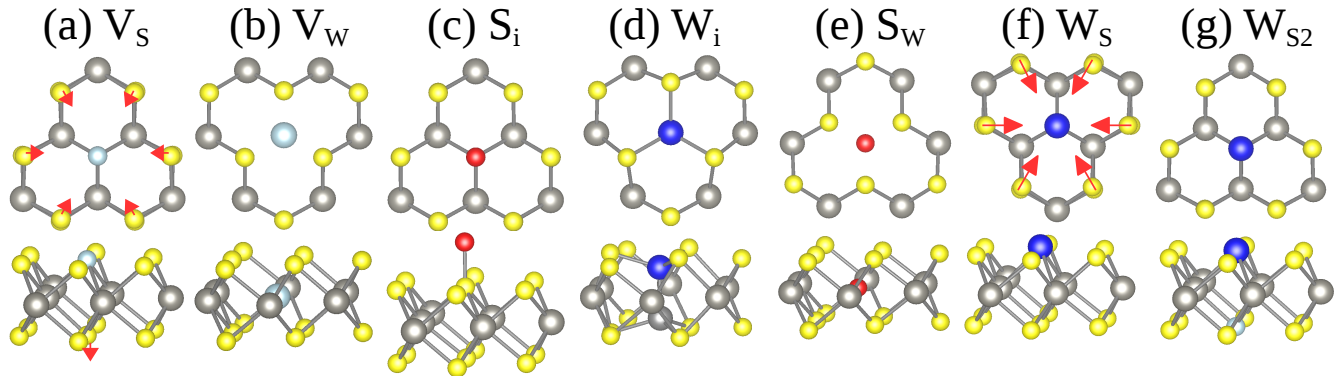


FIG. 2: The relaxed structures of all the defective ML WS₂ supercells. The vacancies are denoted by light blue circles. The defect sulfur atoms are marked in red, and defect tungsten atoms in blue. The arrows indicate the directions and magnitudes of the relaxations.

perimental value of 2.05 eV⁴⁸. In the HSE+SOC calculations only the Γ point was included as we did a test for V_S-WS₂ and W_S-WS₂ and found that a $2 \times 2 \times 2$ k -mesh only improves the band gap for 7 meV for V_S-WS₂, and for 13 meV for W_S-WS₂. Therefore we believe that Γ is sufficient in our case. Our SO splitting of the top valence bands of perfect ML WS₂ calculated by DFT is 430 meV, which is perfectly matching the previous DFT result of 433 meV¹³. HSE increases this splitting considerably to 517 meV.

III. Results and discussion

1. Defect formation energy

The formation energy E_f of a neutral defect is defined as⁴⁹

$$E_f = E_{defect} - E_{perfect} + \sum_i n_i \mu_i. \quad (1)$$

In Eq. 1, E_{defect} is the total energy of the defective system, $E_{perfect}$ is the total energy of the perfect system, n_i is the number of atoms being added (plus) or removed (minus) from the perfect system, and μ_i is the chemical potential of the added or removed atom. The added/removed atom is imagined to be taken from/put to an atomic reservoir, thus the energy required for creating a defect inside a system does not depend only on the system itself, but also on the atomic reservoir, or the surrounding environment. Chemical potentials μ_i are therefore needed to reflect the chemical environment surrounding the system. μ_i is not fixed, but a variable for which we could determine its boundaries by considering the formation reaction of a material. We give the derivation of the boundaries of μ_i in the case of WS₂ in the SM⁵⁰. The final expressions of the boundaries of μ_W and μ_S which are used to calculate the defect formation energies are:

$$E_{WS_2} - 2E_S \leq \mu_W \leq E_W \quad (2a)$$

$$\frac{1}{2}(E_{WS_2} - E_W) \leq \mu_S \leq E_S. \quad (2b)$$

TABLE I: Formation energies (in eV) of the defects selected in this study

	W-rich	S-rich
V _S	1.689	2.897
V _W	6.345	3.928
S _i	2.419	1.211
W _i	5.317	7.733
S _w	8.219	4.594
W _s	5.380	9.005
W _{S2}	6.838	11.671

The calculated defect formation energies are listed in Table I dependent on W-rich or S-rich chemical potentials.

The next step is to choose relevant defect types for further study of the effect of SOC on electronic properties of the defective ML WS₂ slabs. Table I provides a simple criterion in terms of defect formation energy: V_S and S_i possess the lowest formation energies in both the W-rich and S-rich conditions, thus it is sensible to select them for more detailed study. Although the W_S and W_{S2} antisites have a higher formation energy, it has been reported that the MoS and MoS₂ antisites are the predominant point defects in MoS₂ synthesized by physical-vapor-deposition (PVD). Therefore the W_S and W_{S2} antisites are also included in the present study³⁵.

2. Defect state splittings under SOC

As seen in Ref. 51 and Fig. S4 in the SM, the valence bands of MX₂ are composed of the p_x and p_y orbitals of the X atoms (here: S atoms), and the d_{xy} , $d_{x^2-y^2}$ and d_{z^2} orbitals of the M atoms (here: W atoms). The d_{xz} , d_{yz} orbitals are far from the band gap region. Furthermore, Fig. 4 indicates that the top valence bands and the bottom conduction bands consist mainly of the d orbitals of W atoms. The only p orbital present is the p_z orbital from the S atoms, and it does not split under SOC. The calculated BSs with and without SOC are shown in

Fig. 3. We can see from Fig. 3 and Fig. 4 that irrespective of the type of point defects, the VBM of WS_2 always splits into two bands under SOC.

V_S

As discussed in the Introduction, only the W d_{xy} and $d_{x^2-y^2}$ orbitals will undergo SO splitting. This is the case for V_S . The defect states are composed of the linear combinations of W d_{xy} and $d_{x^2-y^2}$ orbitals, which are formerly degenerate are now split into two bands. The magnitude of the SO splitting for V_S is 194 meV. The HSE+SOC calculation gave a SO splitting of 252 meV, which is 58 meV larger than the DFT+SOC value. This substantial energy difference shows the necessity of hybrid functionals in calculating the SO splitting of the defect states.

S_i

In the case of S_i , the only defect state is composed of the p_x and p_y orbitals of the interstitial S atom, which do not split under SOC. This defect state is hidden in the top valence bands.

W_S

For W_S , the defect states are also composed of W d_{xy} and $d_{x^2-y^2}$, but they do not split when SOC is included in the calculations. Further eigenstate analysis shows that the reason for the defect states to be kept degenerate is that the spin projections of these states in the SOC BS are all on the $m_x - m_y$ plane (m_x , m_y and m_z are the magnetization axes), in contrast to the defect states of the other three defect kinds where the spin projections are either mostly on along the m_z axis (in the case of W_{S_2} , $+m_z$ for spin-up and $-m_z$ for spin-down). As a result, the spin states are not split even when SOC is present. We performed a second calculation in which the magnetization was constrained along the m_z axis and thus the defect states indeed split. This allows us to examine the effect of the orientation of magnetization on the defect state splitting. We also found that the m_z -constrained magnetic configuration is 38.9 meV higher in energy (for HSE, the value is 58.4 meV) than the $m_x - m_y$ -relaxed magnetic ground state. This finding suggests that the W_S - WS_2 is a magnetically anisotropic material and that the easy axis lies on the $m_x - m_y$ plane.

In Figs. 3 and 4 we show the BS and the band energies at Γ of the m_z -constrained W_S - WS_2 . There are six defect states for W_S - WS_2 as shown in Fig. 4 (d). Three of these states are spin-up, and the other three are spin-down. For each spin species, the two degenerate states with a lower energy are composed of d_{xy} and $d_{x^2-y^2}$ of the antisite W atom, and the state higher in energy originates from the d_{z^2} orbital. It is worth mentioning that the spin-up d_{xy} and $d_{x^2-y^2}$ orbitals are occupied by two unpaired electrons which are the source of the magnetic moment of W_S - WS_2 as will be discussed in next section. Under SOC, the d_{xy} and $d_{x^2-y^2}$ orbitals split into two bands and each of these bands is a linear combination of d_{xy} and $d_{x^2-y^2}$. For spin-up, this splitting is 296 meV, which is the highest Δ_{SO} among all the WS_2 defects studied in this paper. For spin-down, the splitting is 87 meV. The smaller Δ_{SO} for spin-down may be related to the fact that the spin-down defect states are much higher in energy than the spin-up

states, thus they are closer to the CBM which are the d_{z^2} orbitals that do not exhibit SO splitting. The consequence is that the spin-down defect states are hybridized with the d_{z^2} conduction bands and thus their Δ_{SO} is reduced. This argument is supported by the wave function analysis, which shows that both the d_{xy} and $d_{x^2-y^2}$ orbitals approximately have a $\frac{1}{3}$ d_{z^2} character.

The Δ_{SO} from HSE+SOC are 356 meV and 62 meV for spin-up and spin-down, respectively. With HSE, the SO splitting of the spin-up defect states increases significantly (60 meV) similar to the case of V_S - WS_2 . However, for the spin-down defect states, with HSE the SO splitting decreases by 25 meV. The reason for the decreased Δ_{SO} for spin-down defect states is that HSE pushes these states further into the conduction band region, thereby enhancing the mixing with the d_{z^2} orbitals.

W_{S_2}

W_{S_2} is the most complicated case among the chosen defects. It involves ten defect states - five are spin-up and five are spin-down. As indicated in Fig. 4 (e), without SOC, the five defect states for each spin type can be categorized into three groups: two groups of doubly degenerate states which are lower in energy, and a single d_{z^2} orbital higher in energy. The mixing of the conduction d_{z^2} band with the spin-down d_{xy} and $d_{x^2-y^2}$ defect bands is even worse in the case of W_{S_2} - WS_2 as the spin-down defect d_{z^2} state is already in the conduction band region. The two sets of doubly degenerate states are composed of the linear combinations of the d_{xy} and $d_{x^2-y^2}$ orbitals of the antisite W atom, and will split into four states if SOC is present. Thus, for W_{S_2} - WS_2 , there are four sets of SO splittings. The Δ_{SO} of each split set is 121 meV, 105 meV, 167 meV, and 138 meV, respectively, with ascending energy.

In contrast to DFT, HSE calculation for W_{S_2} - WS_2 relaxed the magnetization onto the $m_x - m_y$ plane. Therefore we again constrained the magnetization along the m_z axis. The constrained configuration is less stable than the relaxed one by 23.5 meV. For the magnetically constrained W_{S_2} - WS_2 , HSE again enhances the splittings which are not close to CBM (the first three splittings in Fig. 4 (e)). The increments are 46 meV, 38 meV, 33 meV, respectively. In contrast, for the fourth splitting HSE decreases Δ_{SO} by 57 meV. One noteworthy feature is that the spin-up splittings are always larger than the spin-down splittings.

3. Magnetic moments of the W_S and W_{S_2} antisites

We found that both W_S and W_{S_2} defects possess a magnetic moment of $2 \mu_B$. This is different from the result of Ref. 35, which indicated that for MoS_2 , only Mo_S - MoS_2 has a magnetic moment but not Mo_{S_2} - MoS_2 . These magnetic moments are generated by the unpaired spin-up electrons residing on the d_{xy} and $d_{x^2-y^2}$ defect states, as indicated by Fig. 4 (d) and (e). These states split under SOC. We defined the spin density as the difference between the spin-up charge density and the spin-down charge density: $\rho = \rho_\uparrow - \rho_\downarrow$ to visualize the magnetic moment distribution around the defect site. The

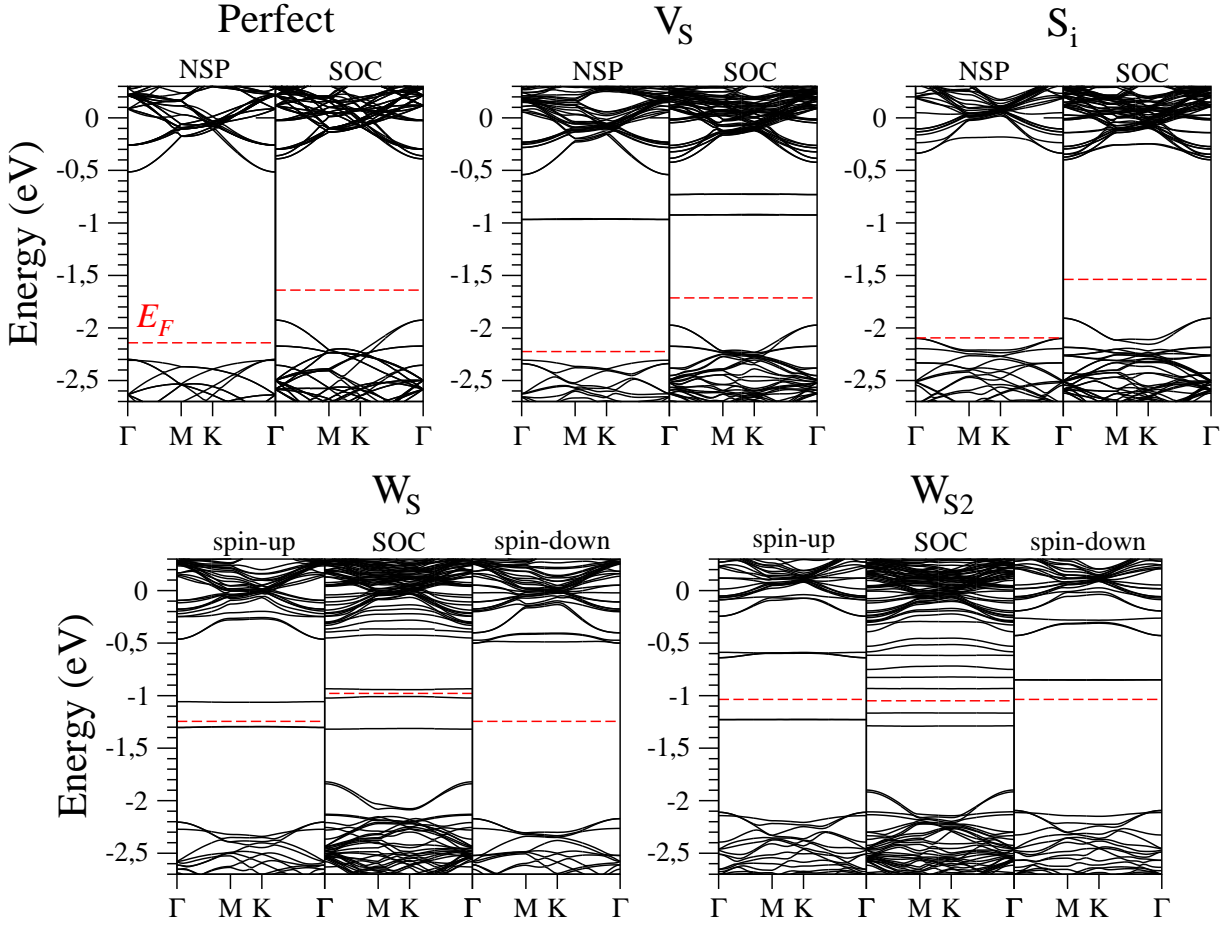


FIG. 3: The band structures calculated with or without SOC for the selected WS_2 slabs. NSP stands for non-spin-polarized non-SOC calculations, and spin-up and spin-down stand for the spin-polarized calculations, respectively. Here the Fermi level is marked in red. The defect state splitting can be clearly seen in the case of V_S and W_S . However, the splitting is suppressed for S_i .

resulting spin density plots are presented for both antisite defects in Fig. 5. At first glance, the magnetic moment seems to be fully localized on the antisite W atom, however for both W_S and W_{S_2} , the d orbitals of the neighboring W atoms contribute to the magnetic moment as well, and to a lesser extent also the next-nearest-neighboring (NNN) W atoms. are involved. For W_{S_2} , the magnetic moment spreads to both the nearest-neighboring (NN) and NNN W atoms.

We compared the ratio between the magnetic moment at the defect W atom and the total magnetic moment ($\mu_r = \frac{\mu(W_{def})}{\mu(all)}$) to give a semi-quantitative description of the distribution of the magnetic moment. We used the VASP default atomic radii for W (1.455 Å) and S (1.164 Å) to perform the spherical integration of the spin density. We calculated μ_r using DFT (spin-polarized), DFT+SOC, and HSE+SOC methods. For W_S , $\mu_r(\text{DFT})=88.4\%$, $\mu_r(\text{DFT+SOC})=88.0\%$, and $\mu_r(\text{HSE+SOC})=98\%$, respectively. For W_{S_2} , the corresponding values were lower at 53.1%, 53.5%, and 66.6%, respectively. In addition, we also found that the magnetic moment distribution shown in Fig. 5 has a triangular shape with a side

length of around 6.4 Å in both cases. Therefore these two antisite defects could also be named magnetic 'superatoms'³⁵.

Therefore one can conclude that, first, for W_S the magnetic moment is almost solely localized on the defect W atom, yet for W_{S_2} the magnetic moment is centered at the defect W atom, but half of it spreads to the NN and NNN W atoms. Second, with the HSE hybrid functional, the magnetic moment is more localized on the defect atom, yielding a higher μ_r .

In order to trace back the origin of these magnetic moments, we compared the total energy and the density of states (DOS) of both the non-spin-polarized (NSP) and spin-polarized (SP) solutions of W_S - WS_2 and W_{S_2} - WS_2 . It was found that the NSP solutions are significantly higher in energy than the SP counterparts. The energy difference $E(\text{SP}) - E(\text{NSP})$ is 402 meV for W_S - WS_2 and 151 meV for W_{S_2} - WS_2 . Therefore both antisite configurations are indeed spin-polarized and are magnetic. The DOS plots of both the NSP and SP solutions for W_S - WS_2 and W_{S_2} - WS_2 in Fig. 6 show clearly the magnetism. By combining Fig. 6, Fig. 4 and the projected DOSs (PDOSs)

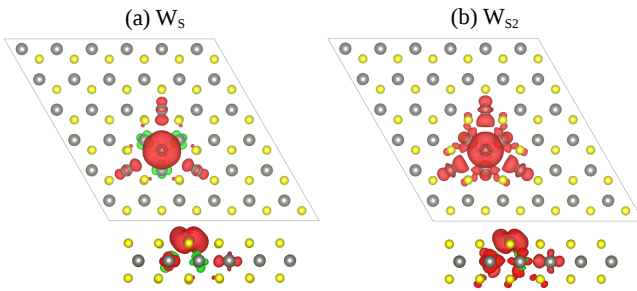


FIG. 5: Spin density plots of (a) W_S and (b) W_{S2} antisites calculated by DFT. The Spin-up charge density is marked in red and the spin-down density in green. The isosurface level is $0.002 \text{ e}/\text{\AA}^3$.

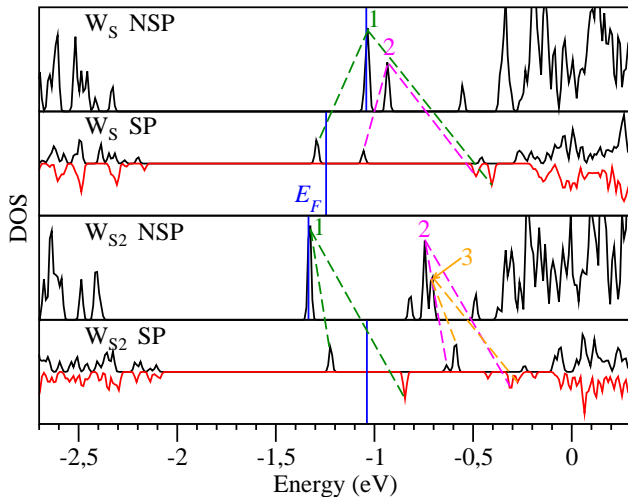


FIG. 6: TDOS plots for both the non-spin-polarized (NSP) and spin-polarized (SP) W_S and W_{S2} antisites. The vertical blue solid lines indicate the Fermi level. The colored dotted lines map the NSP \rightarrow SP splitting of the defect bands

(Fig. S2 in the SM), we performed a thorough eigencharacter analysis of the defect states, revealing that these states are composed of the d orbitals of the antisite W atom which are numbered for each antisite in Fig. 6. For W_S - W_{S2} , group 1 is composed of the d_{xy} and $d_{x^2-y^2}$ orbitals and group 2 is characterized by the d_{z^2} orbital. For W_{S2} - W_{S2} there are three groups of defect states. Group 1 and 2 are both composed of the d_{xy} and $d_{x^2-y^2}$ orbitals. However, they are now mixed with the d_{z^2} orbital to different extents. Group 2 is more heavily mixed with the d_{z^2} orbital than group 1. Group 3 is simply the d_{z^2} orbital. Furthermore, for both antisite defects, only the spin-up part of peak 1 is under the Fermi level and is occupied by two electrons from the d_{xy} and $d_{x^2-y^2}$ orbitals of the antisite W atom. Therefore the magnetism and its origin is confirmed.

IV. Conclusion

In this study we calculated the formation energies of seven different configurations of point defects including monovacancies, interstitials and antisites. We found that among the point defects, V_S and S_i possess the lowest formation energies; $E_f(V_S) = 1.689 \text{ eV}$ in a W-rich chemical environment, and $E_f(S_i) = 1.211 \text{ eV}$ under a S-rich chemical environment. We selected the V_S , S_i , W_S and W_{S2} defects to investigate the SOC band splitting of the defect states. We have shown that the SO splitting depends on both the orbital constitution and the orientation of magnetization of the defect states. The states having the d_{xy} and $d_{x^2-y^2}$ character will undergo significant SO splitting when the magnetization is oriented along the m_z magnetization axis. The as-generated SO splittings are 194 meV for V_S , 296 meV and 87 meV for W_S , and 121 meV, 105 meV, 171 meV, and 138 meV for W_{S2} . The hybrid functional HSE enhances the SO splitting up to 60 meV if the defect state is not close to CBM. However, it decreases the SO splitting up to 57 meV if the defect state is close to CBM. For S_i no SO splitting was found as the defect state is composed solely by the d_{z^2} and p_z orbitals. We also found that not only W_S , but also the W_{S2} defect possesses a local magnetic moment of $2 \mu_B$ around the antisite W atom due to the two unpaired spin-up electrons occupying the d_{xy} and $d_{x^2+y^2}$ defect states. The antisite W atom together with its NN and NNN W atoms thus form the so-called superatom.

The results presented in this Article provide new insights into the SOC behavior of the ML WS_2 containing the most common point defects. These results are expected to be extendable to other ML MX_2 systems. In particular, the controllability of these SO split states are worth further investigation as they are highly promising in spintronics applications. For instance, it would be interesting to examine whether the spins can flip when an electric field is applied. Also, considering the frequent occurrence of the MX_2 antisites generated during the PVD synthesis of the ML MX_2 membranes³⁵, it will be interesting to increase the concentration of MX_2 antisite defects and examine the interaction of the magnetic moments and their arrangement over space. Further development of this topic is beyond the scope of the present paper and will be addressed in future works.

V. Acknowledgements

This project is financially supported by the Dutch science foundation NWO via a VIDI grant (grant number 723.012.006). W.F. Li acknowledges Torbjörn Björkman and Hugo Aramberri for their discussion on the SOC calculations, and Jyh-Pin Chou for his practical instruction on VASP settings and insight of interpreting the SOC band structures.

* Corresponding author: W.F.Li@uu.nl

¹ C. Ataca, H. Şahin, and S. Ciraci, J. Phys. Chem. C **116**, 8983 (2012).

- ² K. F. Mak, C. Lee, J. Hone, J. Shan, and T. F. Heinz, *Phys. Rev. Lett.* **105**, 136805 (2010).
- ³ A. Kuc, N. Zibouche, and T. Heine, *Phys. Rev. B* **83**, 245213 (2011).
- ⁴ Q. H. Wang, K. Kalantar-Zadeh, A. Kis, J. N. Coleman, and M. S. Strano, *Nat. Nanotechnol.* **7**, 699 (2012).
- ⁵ R. Roldán, J. A. Silva-Guillén, P. López-Sancho, F. Guinea, E. Cappelluti, and P. Ordejón, *Ann. Phys. (Berlin)* **526**, 347 (2014).
- ⁶ T. Heine, *Acc. Chem. Res.* **48**, 65 (2015).
- ⁷ R. Ganatra and Q. Zhang, *ACS NANO* **8**, 4074 (2014).
- ⁸ M. Chhowalla, H. S. Shin, G. Eda, L.-J. Li, K. P. Loh, and H. Zhang, *Nat. Chem.* **5**, 263 (2013).
- ⁹ H. Schmidt, F. Giustiniano, and G. Eda, *Chem. Soc. Rev.* **44**, 7715 (2015).
- ¹⁰ Z. Y. Zhu, Y. C. Cheng, and U. Schwingenschlogl, *Phys. Rev. B* **84**, 153402 (2011).
- ¹¹ D. Xiao, G.-B. Liu, W. Feng, X. Xu, and W. Yao, *Phys. Rev. Lett.* **108**, 196802 (2012).
- ¹² X. L. F. Zhang and Q. Niu, *Phys. Rev. B* **84**, 153402 (2011).
- ¹³ K. Kośmider, J. W. González, and J. Fernández-Rossier, *Phys. Rev. B* **88**, 245436 (2013).
- ¹⁴ C. Ataca, H. Şahin, E. Aktürk, and S. Ciraci, *J. Phys. Chem. C* **115**, 3934 (2011).
- ¹⁵ Y. Ma, Y. Dai, M. Guo, C. Niu, J. Lu, and B. Huang, *Phys. Chem. Chem. Phys.* **13**, 15546 (2011).
- ¹⁶ Y. Ding, Y. Wang, J. Ni, L. Shi, S. Shi, and W. Tang, .
- ¹⁷ E. W. K. Koh, C. H. Chiu, Y. K. Lim, Y.-W. Zhang, and H. Pan, *Int. J. Hydro. Energy* **37**, 14323 (2012).
- ¹⁸ J.-W. Wei, Z.-W. Ma, H. Zeng, Z.-Y. Wang, Q. Wei, and P. Peng, *AIP Advances* **2**, 042141 (2012).
- ¹⁹ H. Qiu, T. Xu, Z. Wang, W. Ren, H. Nan, Z. Ni, Q. Chen, S. Yuan, F. Miao, F. Song, G. Long, Y. Shi, L. Sun, J. Wang, and X. Wang, *Nat. Commun.* **4**, 2642 (2013).
- ²⁰ D. Liu, Y. Guo, L. Fang, and J. Robertson, *Appl. Phys. Lett.* **103** (2013).
- ²¹ A. Carvalho and A. H. C. Neto, *Phys. Rev. B* **89**, 081406(R) (2014).
- ²² J. Chang, S. Larentis, L. F. R. Emanuel Tutuc, and S. K. Banerjee, *Appl. Phys. Lett.* **104**, 141603 (2014).
- ²³ S. Yuan, R. Roldán, M. I. Katsnelson, and F. Guinea, *Phys. Rev. B* **90**, 041402(R) (2014).
- ²⁴ P. Rastogi, S. Kuma, S. Bhowmick, A. Agarwal, and Y. S. Chauhan, *J. Phys. Chem. C* **118**, 30309 (2014).
- ²⁵ S.-C. Lu and J.-P. Leburton, *Nanoscale Res. Lett.* **9**, 676 (2014).
- ²⁶ P. K. Chow, R. B. Jacobs-Gedrim, J. Gao, T.-M. Lu, B. Yu, H. Terrones, and N. Koratkar, *ACS Nano* **9**, 1520 (2015).
- ²⁷ H. Liu, N. Han, and J. Zhao, *RSC Adv.* **5**, 17572 (2015).
- ²⁸ A.-M. Hu, L. ling Wang, W.-Z. Xiao, G. Xiao, and Q.-Y. Rong, *Comp. Mater. Sci.* **107**, 72 (2015).
- ²⁹ W. Zhao, Z. Ghorannevis, L. Chu, M. Toh, C. Kloc, P.-H. Tan, and G. Eda, *ACS NANO* **7**, 791 (2012).
- ³⁰ H. Li, S. Liu, S. Huang, D. Yin, C. Li, and Z. Wang, *Ceram. Int.* **42**, 2364 (2015).
- ³¹ Z. Liu, K. Suenaga, Z. Wang, Z. Shi, E. Okunishi, and S. Iijima, *Nat. Commun.* **2**, 213 (2011).
- ³² H.-P. Komsa, J. Kotakoski, S. Kurasch, O. Lehtinen, U. Kaiser, and A. V. Krasheninnikov, *Phys. Rev. Lett.* **109**, 035503 (2012).
- ³³ H.-P. Komsa, S. Kurasch, O. L. U. Kaiser, and A. V. Krasheninnikov, *Phys. Rev. B* **88**, 035301 (2013).
- ³⁴ W. Zhou, X. Zou, S. Najmaei, Z. Liu, Y. Shi, J. Kong, J. Lou, P. M. Ajayan, B. I. Yakobson, and J.-C. Idrobo, *Nano Lett.* **13**, 2615 (2013).
- ³⁵ J. Hong, Z. Hu, M. Probert, K. Li, D. Lv, X. Yang, L. Gu, N. Mao, Q. Feng, L. Xie, J. Zhang, D. Wu, Z. Zhang, C. Jin, W. Ji, X. Zhang, J. Yuan, and Z. Zhang, *Nat. Commun.* **6**, 6293 (2015).
- ³⁶ J.-Y. Noh, H. Kim, and Y.-S. Kim, *Phys. Rev. B* **89**, 205417 (2014).
- ³⁷ H.-P. Komsa and A. V. Krasheninnikov, *Phys. Rev. B* **91**, 125304 (2015).
- ³⁸ S. Haldar, H. Vovusha, M. K. Yadav, O. Eriksson, and B. Sanyal, *Phys. Rev. B* **92**, 235408 (2015).
- ³⁹ G. Kresse and J. Hafner, *Phys. Rev. B* **49**, 14251 (1994).
- ⁴⁰ G. Kresse and J. Furthmüller, *Comput. Mat. Sci.* **6**, 15 (1996).
- ⁴¹ G. Kresse and J. Furthmüller, *Phys. Rev. B* **54**, 11169 (1996).
- ⁴² P. Blochl, *Phys. Rev. B* **50**, 17953 (1994).
- ⁴³ J. Perdew, K. Burke, and M. Ernzerhof, *Phys. Rev. Lett.* **77**, 3865 (1996).
- ⁴⁴ J. Perdew, K. Burke, and M. Ernzerhof, *Phys. Rev. B* **78**, 1396 (1997).
- ⁴⁵ J. Klimeš, D. R. Bowler, and A. Michaelides, *J. Phys.: Condens. Matter* **22**, 022201 (2010).
- ⁴⁶ Please refer to the Supplementary Information for more details.
- ⁴⁷ A. V. Krukau, O. A. Vydrov, A. F. Izmaylov, and G. E. Scuseria, *J. Chem. Phys.* **125**, 224106 (2006).
- ⁴⁸ G. L. Frey, R. Tenne, M. J. Matthews, M. S. Dresselhaus, and G. Dresselhaus, *J. Mater. Res.* **13**, 2412 (1998).
- ⁴⁹ C. G. V. de Walle and J. Neugebauer, *J. Appl. Phys.* **95**, 3851 (2004).
- ⁵⁰ Please refer to Section II in the SM for more information.
- ⁵¹ J. E. Padilha, H. Peelaers, A. Janotti, and C. G. V. de Walle, *Phys. Rev. B* **90**, 205420 (2014).